BIOCHEMISTRY
including biophysical chemistry & molecular biology

Article

pubs.acs.org/biochemistry

Structural and Functional Characterization of Aerobactin Synthetase IucA from a Hypervirulent Pathotype of *Klebsiella pneumoniae*

Daniel C. Bailey,[†,‡,§] Eric J. Drake,[†,§] Thomas D. Grant,[†,§] and Andrew M. Gulick*[,†,§]

[†]Department of Structural Biology and [‡]Medical Scientist Training Program, The Jacobs School of Medicine & Biomedical Sciences, State University of New York at Buffalo, Buffalo, New York, United States

[§]The Hauptman-Woodward Medical Research Institute, Buffalo, New York, United States

ABSTRACT: Iron is a vital mineral nutrient required by virtually all life forms to prosper; pathogenic bacteria are no exception. Despite the abundance of iron within the human host, highly regulated iron physiology can result in exceedingly low levels of iron bioavailable to prospective invading bacteria. To combat this scarcity of iron, many pathogenic bacteria have acquired specific and efficient iron acquisition systems, which allow them to thrive in iron-deficient host environments. One of the more prominent bacterial iron acquisition systems involves the synthesis, secretion, and reuptake of small-molecule iron chelators known as siderophores. Aerobactin, a citrate-hydroxamate siderophore originally isolated nearly 50 years ago, is produced by a number of pathogenic Gram-negative bacteria. Aerobactin has recently been demonstrated to play a pivotal role in mediating the enhanced virulence of a particularly invasive pathotype of *Klebsiella pneumoniae* (hvKP). Toward further understanding of this key virulence factor, we report the structural and functional characterization of aerobactin synthetase IucA from a strain of hvKP. The X-ray crystal structures of unliganded and ATP-bound forms of IucA were solved, forming the foundation of our structural analysis. Small angle X-ray scattering (SAXS) data suggest that, unlike its closest structurally characterized homologues, IucA adopts a tetrameric assembly in solution. Finally, we employed activity assays to investigate the substrate specificity and determine the apparent steady-state kinetic parameters of IucA.

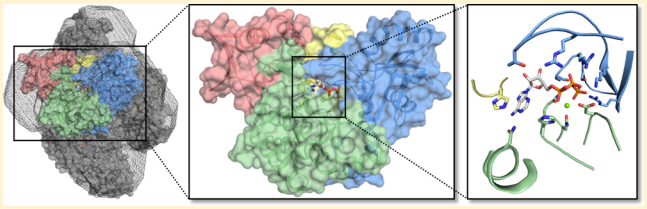

Iron is the fourth most abundant element by mass in Earth's crust. As a transition metal, iron exists as a redox pair consisting of the reduced ferrous (Fe^{2+}) and the oxidized ferric (Fe^{3+}) species in most physiologic environments. This redox activity is what makes iron so valuable and underlies its utilization in a variety of physiologic processes including photosynthesis, respiration, nitrogen fixation, oxygen transport, and DNA synthesis.[1] Except for a few primitive bacteria, iron is a vital mineral nutrient required by essentially all life forms to survive and thrive. With this strict requirement for iron, it has been estimated that bacteria require an iron concentration on the order of 10^{-6} M in order to sustain growth.[2] Despite the seeming abundance of iron in the environment, maintaining intracellular iron levels above this threshold is no trivial task for most organisms, including pathogenic bacteria. Failing to secure sufficient quantities of this vital nutrient can limit the ability of the pathogenic bacteria to establish an infection.

Human physiology tightly regulates iron metabolism, thereby limiting the amount of free iron in the body.[3,4] There are two principal reasons for such tight iron regulation. First, limiting free iron reduces the unwanted generation of damaging reactive oxygen species (ROS). Second, the innate immune system utilizes a variety of acute phase iron regulatory proteins (i.e., hepcidin, ferritin, lactoferrin, haptoglobin, etc.) to exert iron nutritional immunity during infection and inflammation.[3] Highly regulated iron metabolism results in exceedingly low concentrations of free iron within the host that is available to an invading pathogen, with serum concentrations estimated to be as low as 10^{-24} M.[2]

With a scarcity of iron to contend with, evolution has selected for microbes that have acquired highly efficient and specific systems for iron assimilation. Iron acquisition systems are widely recognized as virulence factors in many pathogenic bacteria, allowing them to multiply and cause infection within the iron-deficient host environment.[5−7] One of the more prominent iron acquisition systems employed by bacteria is the use of small molecule iron chelators known as siderophores. The ability to synthesize certain siderophores has been strongly associated with virulence in a number of pathogenic bacteria, including *Escherichia coli*,[8] *Pseudomonas aeruginosa*,[9] *Bacillus anthracis*,[10] *Mycobacteria tuberculosis*,[11] *Yersinia pestis*,[12] and *Klebsiella pneumoniae*.[13]

Klebsiella pneumoniae (KP) is a relatively common human pathogen, with "classical" pathotypes (cKP) historically responsible for establishing infection in susceptible individuals with compromised immune systems, often in the setting of hospitals and other long-term care facilities.[14] Strains of cKP have recently captured the attention of the medical community due to their acquisition of extreme drug resistance.[15] In an equally alarming development, beginning in the mid 1980s in

Received: April 28, 2016
Revised: June 2, 2016
Published: June 2, 2016

DOI: 10.1021/acs.biochem.6b00409
Biochemistry 2016, 55, 3559−3570

the Asian Pacific Rim, the medical community began observing serious KP infections occurring in healthy, ambulatory individuals in the community. Over the last 30 years, this now recognized "hypervirulent" KP pathotype (hvKP) has disseminated across the globe, causing life-threatening cases of severe pneumonia, hepatic and various non-hepatic abscesses, meningitis, endopthalmitis, and necrotizing fasciitis.[16,17] There is fear among medical professionals that the confluence of extreme drug resistant and hypervirulent KP pathotypes could lead to a genuine "superbug", a pathogen that is extremely difficult to treat and causes serious life-threatening infections.[18]

Recent investigations have demonstrated that the enhanced virulence of hvKP is, in large part, mediated by its enhanced iron acquisition ability.[19,20] Despite containing genes for the biosynthesis of four different siderophores (enterobactin [encoded by the *ent* operon], salmochelin [*iro*], yersiniabactin [*irp*], and aerobactin [*iuc*]), it is hvKP's ability to overexpress *only* aerobactin that is responsible for mediating the enhanced virulence of hvKP *in vitro* and *in vivo*. Isogenic mutants of aerobactin synthesis, but not of the other three siderophores alone or in combination, showed drastically reduced virulence in murine infection models.[21]

First isolated in 1969,[22] the aerobactin iron acquisition system has been widely studied over the intervening decades. Aerobactin was the earliest characterized example of a nonribosomal peptide synthetase (NRPS)-independent siderophore (NIS).[23,24] The aerobactin system consists of four biosynthetic enzymes (IucA-D, "iron uptake chelate") and an outer membrane transporter (IutA, "iron uptake transport"). The aerobactin biosynthetic pathway[25] (Scheme 1A) begins

Scheme 1

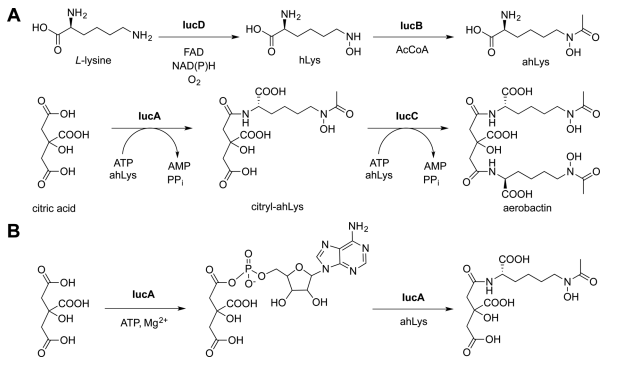

with the N^6 hydroxylation of L-lysine to yield N^6-hydroxy-L-lysine (hLys). Next, an acetyl group is transferred from acetyl-CoA to the N^6 position of hLys by the acetyltransferase IucB, to yield N^6-acetyl-N^6-hydroxy-L-lysine (ahLys). Finally, 2 equiv of ahLys are sequentially installed on the primary carboxyl groups of citrate by the NIS synthetases IucA and IucC to yield aerobactin. IucA is the prototypical Type A NIS synthetase, which utilize citrate as a substrate (Scheme 1B), while IucC is the prototypical Type C NIS synthetase, which employ a citrate derivative as their substrate. Despite being among the earliest known examples, IucA and IucC have yet to be structurally or functionally characterized.[25] However, the family of NIS synthetases has recently garnered increased attention as researchers have sought to better understand the enzymology of siderophore biosynthesis. This includes the recent structural and functional characterization of the Type A NIS synthetase AcsD (achromobactin, *Pectobacterium chrysanthemi*), and the two Type C NIS synthetases AsbB (petrobactin, *Bacillus anthracis*) and AlcC (alcaligin, *Bordetella bronchiseptica*).[26−29]

Herein, we report the structural and functional characterization of the archetypal Type A NIS synthetase IucA from a strain of hvKP (hvKP1).[30] Our structural characterization is centered on the X-ray crystal structures of unliganded and ATP-bound forms of IucA. Combined with the X-ray crystal structures, the quaternary structure of hvKP IucA was investigated using small-angle X-ray scattering (SAXS), demonstrating that hvKP IucA exists as a tetramer in solution. This conclusion is in contrast to the three other structurally characterized NIS synthetases, which have all been reported to be biological dimers.[26,28] Evaluating the enzymatic activity of hvKP IucA allowed us to determine its apparent kinetic parameters and, together with the structural data, draw conclusions about its molecular catalytic mechanism. As a whole, this work helps define a potential "antivirulence" therapeutic target against hvKP, an antimicrobial strategy that has recently been gaining traction for a number of potential benefits.[31] Finally, our structural and functional characterization of hvKP IucA further contributes to the understanding of the fundamental enzymology of the widely distributed NIS synthetase family of enzymes.

EXPERIMENTAL METHODS

Cloning, Expression, and Purification of hvKP IucA. The 574-residue IucA protein from hypervirulent *K. pneumoniae* hvKP1 is present in the Genbank database at accession EMB09144.1. A comparison of IucA sequences available in *Klebsiella* and homologous species yields two distinct clusters of protein lengths that result from variable selection of the starting methionine codon. In *K. pneumoniae*, IucA proteins are reported with either 574 or 593 residues. Expression plasmids producing both versions of IucA were generated. Attempts to express and purify soluble hvKP1 IucA failed with the 593 residue isoform, but were successful with the 574 residue version. This, combined with homology analysis of IucA in other related Gram-negative enteric bacteria led us to conclude that the 574 amino acid sequence is the "true" hvKP IucA protein and to use the 574 residue hvKP1 construct for all of the subsequent analyses and experiments.

The *iucA* gene was amplified from hvKP genomic DNA (hvKP1[30]) using primers to incorporate restriction sites at the 5′ and 3′ ends of the gene. The gene was subcloned into a modified pET15b vector containing an *N*-terminal 5xHis tag and a TEV protease recognition site. The expression construct was verified by DNA sequencing analysis. The expression vector was transformed into an *E. coli* BL21(DE3) expression cell line for protein production. Cells were grown in LB media at 37 °C (250 rpm) for approximately 3 h to an OD_{600} of ≈0.55−0.65. IucA expression was induced with the addition of 500 μM IPTG, followed by incubation at 16 °C (250 rpm) for ≈18 h. Cells were harvested by centrifugation at $6 \times 10^3 g$ for 15 min at 4 °C. After decanting off the supernatant media, the cell pellet was flash frozen in N_2 (l) and stored at −80 °C for later use. Selenomethionine-labeled IucA was expressed using a similar protocol, except that cells were grown in M9 minimal media supplemented with an amino acid cocktail that included selenomethionine.[32]

Five grams of frozen cell pellet were resuspended in 45 mL of lysis buffer (50 mM HEPES, 250 mM NaCl, 10 mM imidazole, 0.2 mM TCEP, 10% glycerol, pH 7.5). After agitating with 50 mg of lysozyme for 30 min at 4 °C, cell lysis was carried out by

DOI: 10.1021/acs.biochem.6b00409
Biochemistry 2016, 55, 3559−3570

Table 1. Data Collection and Refinement Statistics[a]

	IucA	IucA w/ATP	SeMet IucA (MAD)		
Data Collection					
beamline	APS 23-ID-B	APS 23-ID-B	SSRL 7-1	SSRL 7-1	SSRL 7-1
wavelength (Å)	0.96802	1.03320	λ_1 (peak) 0.97892	λ_2 (inflection) 0.97953	λ_3 (remote) 1.01623
space group	$P6_222$	$P2_1$	$P6_222$	$P6_222$	$P6_222$
unit cell *a*, *b*, *c* (Å)	106.79, 106.79, 264.72	170.85, 96.63, 173.23	106.38, 106.38, 264.54	106.40 106.40 264.63	106.37 106.37 264.62
α, β, γ (deg)	90, 90, 120	90, 90.02, 90	90, 90, 120	90, 90, 120	90, 90, 120
IucA molecules/ASU	1	8	1	1	1
resolution range (Å)	52.34−2.4 (2.49−2.4)	49.57−2.2 (2.28−2.2)	29.91−3.1 (3.40−3.1)	29.92−3.2 (3.42−3.2)	29.91−3.2 (3.42−3.2)
total reflections	342,481 (34,020)	1,128,642 (111,155)	114,036 (27,646)	103,466 (19,044)	103,481 (18,993)
unique reflections	35,840 (3,507)	283,617 (28,004)	16,892 (3,934)	15,418 (2,722)	15,402 (2,712)
multiplicity	9.6 (9.7)	4.0 (4.0)	6.8 (7.0)	6.7 (7.0)	6.7 (7.0)
completeness (%)	100.0 (100.0)	99.2 (98.5)	99.8 (100.0)	99.8 (100.0)	99.8 (99.9)
mean $I/\sigma(I)$	14.26 (2.77)	7.62 (3.15)	12.9 (4.8)	13.8 (5.5)	13.6 (5.4)
R_{MERGE}	0.0927 (0.7252)	0.1194 (0.4555)	0.109 (0.363)	0.109 (0.337)	0.107 (0.339)
R_{MEAS}	0.0980 (0.7663)	0.1379 (0.5630)	0.133 (0.426)	0.118 (0.365)	0.116 (0.366)
*CC*1/2	0.999 (0.880)	0.995 (0.796)	0.996 (0959)	0.997 (0.968)	0.997 (0.968)
*CC**	1.000 (0.967)	0.999 (0.941)			
Structure Refinement					
R_{WORK}	0.2130 (0.2907)	0.2139 (0.2639)			
R_{FREE}	0.2548 (0.3518)	0.2490 (0.2969)			
no. protein/ligand atoms	4,306/5	34,712/256			
RMSD bond lengths (Å)	0.009	0.005			
RMSD bond angles (deg)	1.069	1.019			
Wilson *B*-factor (Å^2)	46.1	19.9			
average *B*-factor (Å^2)					
protein	53.7	29.6			
ligand	67.1	20.1			
Ramachandran analysis					
favored (%)	97.2	96.0			
allowed (%)	2.4	3.4			
outliers (%)	0.4	0.6			
rotamer outliers (%)	0.5	0.7			
MolProbity Clashscore	5.3	3.26			
PDB code	5JM7	5JM8			

[a]Values in parentheses are for the highest resolution shell.

sonication (5 cycles × 30 s). The resulting slurry was separated by ultracentrifugation at 185 × 10^3*g*. The supernatant was filtered over a 0.45 μm polysulfone membrane before being subjected to immobilized metal affinity chromatography (IMAC). The lysate supernatant was passed over a 5 mL Ni^{2+}-Sepharose column (HisTrap HP, GE Healthcare Life Sciences). Following a wash with buffer containing 50 mM imidazole, bound proteins were eluted from the column using lysis buffer plus 300 mM imidazole. Fractions that were shown to contain His-tagged IucA by SDS-PAGE were combined and dialyzed overnight at 4 °C with TEV protease in dialysis buffer (50 mM HEPES, 250 mM NaCl, 0.2 mM TCEP, 0.5 mM EDTA, 10% glycerol, pH 7.5). Following TEV protease cleavage, a glycine and a histidine amino acid remain upstream of the starting methionine residue. After spiking with imidazole to 20 mM, the dialyzed sample was passed over the Ni^{2+}-Sepharose column for a second time. The flow through fractions containing IucA without the His tag were combined and concentrated using a 30 000 MWCO filter (Amicon Ultra-15) before being subjected to size exclusion chromatography (SEC). The concentrated protein solution was eluted over the SEC column (HiLoad 16/60 Superdex 200, GE Healthcare Life Sciences) using an eluant of 50 mM HEPES, 150 mM NaCl, 0.2 mM TCEP, pH 7.5 at a flow rate of 1 mL/min. The desired fractions were combined and dialyzed into a final buffer of 25 mM HEPES, 75 mM NaCl, 0.2 mM TCEP, pH 7.5, concentrated to ≈10 mg/mL, and flash frozen in N_2 (l) before being stored at −80 °C for subsequent use. All subsequent experiments and analyses were conducted with IucA diluted in this final buffer. To generate the size exclusion chromatogram shown in Figure 4C, 0.5 mL of ∼1 mg/mL purified IucA was eluted over the same Superdex 200 column using identical conditions. The molecular weight standard curve shown in Figure 4D was generated with protein standards (Sigma-Aldrich, MWGF200) following the manufacturer's protocol and using the same column and conditions as above.

Crystallization of IucA. Conditions for the crystallization of native and SeMet-labeled IucA were initially identified using the microbatch crystallization screening service at the Hauptman-Woodward Medical Research Institute.[33] The initial lead

DOI: 10.1021/acs.biochem.6b00409
Biochemistry 2016, 55, 3559−3570

conditions were optimized using a hanging drop vapor diffusion method. The optimized crystallization conditions for both native and SeMet IucA were 1:1 protein (~5.5 mg/mL) to cocktail (500−750 mM ammonium sulfate, 100−250 mM potassium−sodium tartrate, 100 mM sodium citrate pH 5.6) incubated at 14 or 20 °C for 3−7 days. The resulting bipyramidal crystals were mounted in nylon loops and cryoprotected by serial transfer through solutions of crystallization cocktail plus 8, 16, and 24% (v/v) ethylene glycol. The crystals were then flash frozen in N_2 (l) before being shipped to the synchrotron for data collection.

Lead conditions for the crystallization of native IucA with ATP bound were identified using an in-house hanging-drop vapor diffusion screen. The optimized conditions were 1:1 protein (~5.5 mg/mL preincubated with 1 mM ATP and $MgCl_2$ for 1 h) to cocktail (15−32% PEG 400, 100 mM MES pH 6.0) incubated at 14 °C for 3−7 days. The resulting rhombohedral crystals were either cryoprotected with additional PEG 400 up to 28% (v/v) or directly flash frozen in N_2 (l), before being shipped to the synchrotron for data collection.

X-ray Data Collection, Structure Determination, and Refinement. Data sets were collected remotely at both the Advanced Photon Source (APS, GM/CA 23-ID-B) and the Stanford Synchrotron Radiation Lightsource (SSRL, 7-1). The initial phases were obtained from SeMet protein and MAD phasing. Subsequent native structures were solved using molecular replacement and the SeMet model (Phaser[34]). Diffraction data were processed using iMosflm,[35] automated model building using PHENIX.Autobuild,[36] manual model building and refinement using Coot,[37] and automated refinement using PHENIX.Refine.[38] Data collection and refinement statistics can be found in Table 1.

Despite attempts to index the IucA with ATP data set in orthorhombic $C222_1$ and $P2_12_12_1$ space groups, the *R*-factors persisted at higher than expected values, and the electron density maps displayed inconsistencies during structure refinement. Reanalysis of the data in lower symmetry space groups suggested that the IucA with ATP crystal was pseudomerohedrally twinned, with a twin fraction of approximately 45% and a β angle of 90°. The combination of reindexing the data in monoclinic $P2_1$ and refining using the twin law *h*, −*k*, −*l*, yielded substantially better *R*-factors as well as a more consistent electron density map. Superposition of the eight monomers from the structure showed no significant variation in the individual chains, and we believe the improved refinement derives from minor variations in the positioning of the tetramers in the lattice that approximate the higher symmetry space groups. The electron density of the thumb domain, specifically residues 25−104, of chains F and H is significantly worse than the remaining chains. Several loops/turns with poor omit map density were left in place as inclusion resulted in modest $2F_O - F_C$ density. Removal of these loops altogether reduced the R_{work} but had no impact on the R_{free} values. The final model therefore contains these loops; analysis was done with the more complete protein chains. The structure factors and coordinates for unliganded (5JM7) and ATP-bound IucA (5JM8) have been deposited within the Protein Data Bank.

Docking of ahLys in the active site of IucA was carried out using Auto Dock Vina software.[39]

Small Angle X-ray Scattering (SAXS). SAXS data on native hvKP IucA were collected at SSRL beamline 4-2.[40,41] Protein samples (40 μL total volume) were prepared in a dilution series of 5.30, 3.98, 2.65, 1.33, 0.66, 0.40, and 0.13 mg/mL in a buffer of 25 mM HEPES, 75 mM NaCl, and 0.1 mM TCEP. In order to investigate the effect of ATP binding on IucA's conformation, a second dilution series (5.05, 3.79, 2.53, 1.26, 0.63, 0.38, 0.13 mg/mL IucA) was prepared in an identical buffer system plus 1 mM ATP and $MgCl_2$. Because of a reduction in the S/N ratio of the scattering data and increased error in sample preparation, only data from the four highest enzyme concentrations were employed in particle size calculations. Each sample was held at 10 °C, and data were collected with 20 exposures of one second duration (λ = 1.12713 Å). Scattering from a buffer blank was subtracted from the data. The scattering curves were produced using SASTool software,[41] and the scattering curves were analyzed using software from the ATSAS program package:[42] PRIMUSQT, DAMMIF, DAMAVER, CRYSOL, SUPCOMB, and DATVC. Guinier analysis ($0.4 \leq qR_G \leq 1.3$) was used to determine the zero-angle scattering intensity (I_0). This value was then used to calculate the molecular weight by employing lysozyme (14.3 kDa, 16.3 mg/mL) as a reference standard. For molecular weight calculations based on Porod volume (*PV*), the pair distance distribution ($P(r)$) function ($q \leq 0.3$) was employed to calculate the *PV*, which was then divided by 1.66 to yield the molecular weight in daltons.[43] The DATVC software was used to calculate the molecular weight by the volume of correlation (V_C) including data for $q \leq 0.3$. The IucA *ab initio* molecular envelope was calculated using P222 symmetry restraints in DAMMIF and including data for $q \leq 0.3$. Ten *ab initio* envelopes were reconstructed with DAMMIF and averaged with DAMAVER. The CRYSOL scattering curves were calculated using a solvent electron density of 0.390 electrons/Å^3, a value which was empirically determined to yield the best correlation between the experimental and calculated curves. To correct for a slight concentration dependence (minor interparticle repulsion) in the SAXS data, PRIMUSQT was used to generate scattering curves extrapolated to infinite dilution.

NADH Consumption Assay. An NADH consumption assay[44] was used to measure the activity of native hvKP IucA. In this assay, IucA catalyzes the condensation of citrate and hydroxylamine, serving as a surrogate nucleophile, to produce the corresponding citryl hydroxamate, PP_i, and AMP. The enzymes adenylate kinase (myokinase), pyruvate kinase, and lactate dehydrogenase couple the production of AMP to the oxidation of NADH to NAD^+, which is followed by monitoring NADH's absorption maximum at 340 nm (ε = 6220 M^{-1} cm^{-1}).

To carry out the assay, 90 μL of master mix was combined with 10 μL of 20 μM IucA to yield a reaction mixture containing 50 mM HEPES pH 7.5, 15 mM $MgCl_2$, 100 mM hydroxylamine, 3 mM phosphoenolpyruvate, 5 mM ATP, 5 mM sodium citrate, 200 μM NADH, 10 U/mL adenylate kinase, pyruvate kinase, and lactate dehydrogenase, and 2 μM IucA. To determine the apparent steady state kinetic parameters of each substrate, the concentration of a single substrate was varied while the others were maintained at saturating concentrations. The reactions were carried out in triplicate at 37 °C in 96-well clear polystyrene plates, and the absorbance at 340 nm was measured using a Biotek Synergy 4 plate reader. The maximum initial absorbance slopes were converted to enzyme activity and plotted versus varying substrate concentrations. The plot of enzyme activity versus substrate concentration was fitted with a best-fit nonlinear regression line using Graphpad Prism software in order to

DOI: 10.1021/acs.biochem.6b00409
Biochemistry 2016, 55, 3559−3570

approximate the K_M and k_{cat} values. When testing the activity of IucA with assorted potential nucleophiles, each was evaluated at a concentration of 50 mM. Control reactions demonstrated that L-lysine, N^6-acetyl-L-lysine, and L-arginine do not inhibit the coupling enzymes myokinase, pyruvate kinase, and lactate dehydrogenase at concentrations up to 50 mM.

Ferric Hydroxamate Assay. In order to evaluate the activity of hvKP IucA with various carboxylic acid substrates, we employed a ferric hydroxamate detection assay.[45,46] A 100 μL reaction mixture consisting of 50 mM HEPES pH 7.5, 15 mM $MgCl_2$, 150 mM hydroxylamine, 3 mM ATP, 3 mM carboxylic acid substrate, and 2 μM IucA was added to a clear polystyrene 96-well plate and allowed to react for 90 min at room temperature (~23 °C). To quench and develop the reaction mixture, 100 μL of solution containing 10% w/v $FeCl_3 \cdot 6H_2O$ and 0.7 M HCl was added. After the plate was shaken and the analyte solution was allowed to equilibrate for 1 min, the absorbance at 540 nm was measured using a Biotek Synergy 4 plate reader. Each carboxylic acid substrate was assayed using seven replicates, and a control that included citrate and heat-inactivated IucA (95 °C for 2 min) was used to blank the experimental replicates.

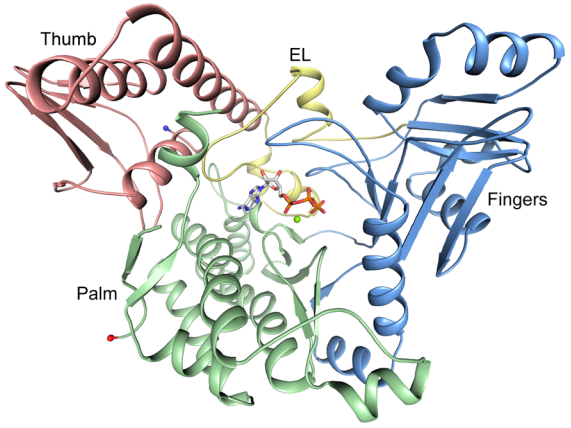

Figure 1. X-ray crystal structure of the IucA protomer with ATP and a Mg^{2+} ion bound in its active site. The peptide backbone is depicted in the ribbon diagram and colored by domain: thumb, salmon; extended loop (EL), yellow; fingers, light blue; and palm, pale green. All subsequent structures are colored using this domain color scheme. The N- and C-termini are colored as blue and red spheres, respectively.

RESULTS

Tertiary Structure of the IucA Protomer. The X-ray crystal structures of unliganded and ATP-bound forms of IucA were solved to 2.4 and 2.2 Å resolution, respectively (Table 1). We first solved the unliganded IucA in the hexagonal space group $P6_222$ with a single protomer in the asymmetric unit. The final unliganded IucA model consists of 548 of the total 574 residues in the protein. The 26 unmodeled residues include 1−8, 281−288, 550−556, and 572−574. In addition to the protein chain, a sulfate ion was modeled in the active site occupying the expected binding location of the phosphates of the ATP substrate. The IucA with ATP crystal was pseudomerohedrally twinned and solved in the monoclinic space group $P2_1$ with eight protein chains in the asymmetric unit. The ATP-bound IucA model contains 550−556 residues across the eight chains. Unmodeled gaps in the peptide chain include 1−8, 550−557, and 572−574, with minor variations among the eight chains. An ATP molecule and a Mg^{2+} ion are modeled in the active site of all eight protomers. Despite considerably different crystallization conditions, the unliganded and ATP-bound IucA models are nearly identical, with an average RMSD of 0.65 Å over 542 α-carbons (the apo IucA protomer compared to each of the eight IucA with ATP protomers). Furthermore, the overall fold of the unliganded IucA protomer was found to be quite similar to the previously structurally characterized unliganded NIS synthetases despite sharing relatively low sequence homology (AcsD RMSD = 3.1 Å over 520 α-carbons, 23% identical; AsbB = 4.0 Å over 496, 18%; and AlcC = 3.6 Å over 496, 19%).

The IucA protomer displays a "cupped hand" topology that can be divided into three distinct domains, the (1) thumb, (2) fingers, and (3) palm, following the notation originally coined by Schmelz et al.[28] (Figure 1). The thumb domain (salmon, 9−122) consists of a three-helix bundle bordered by a five-stranded antiparallel β-sheet. The thumb domain does not contribute any residues to the active site. Connecting the thumb and fingers domain is an intervening sequence ("EL" region, yellow, 123−174) that contains an extended loop (141−161) and three short α-helices. This extended loop reaches into the interior of the enzyme and borders the active site. The core of the fingers domain (light blue, 175−357) consists of a four-stranded antiparallel β-sheet that is decorated with α-helices, β-strands, and loops. A loop from the fingers domain contains several residues that interact with the phosphates of ATP. Another loop extends over the top of the active site, forming a "lid" over the bound ATP molecule. In the unliganded IucA crystal structure, this loop was unresolved from residues 281−288. However, coordination of ATP in the active site caused this loop to become fully resolved. This suggests that ATP coordination causes a conformational change in which this otherwise mobile lid loop becomes much more constrained over the top of the active site. The palm domain (pale green, 358−572) forms the floor of the active site and acts as the bridge connecting the thumb and fingers domain. Two loops from the palm domain contribute residues that help coordinate ATP and the Mg^{2+} ion. A sequence of about eight residues (550−557) toward the C-terminus is unresolved in both IucA crystal structures. The corresponding region in the AcsD and AlcC crystal structures also contain unresolved residues, suggesting that this region has inherent flexibility.

Active Site. The active site of IucA is located in the central depression at the center of the cupped hand topology. The robust electron density in the active site of all eight protomers in the asymmetric unit allowed the conformation of ATP and the Mg^{2+} ion to be unambiguously modeled (Figure 2A). The EL region, the palm domain, and the fingers domain all contribute residues to the active site. As illustrated in Figure 2A, ATP and Mg^{2+} are coordinated deep in the active site through numerous specific interactions. The adenosine ring system is stacked with His147 and hydrogen bonded to Asn487. The phosphates are bound in a positively charged pocket and interact with Ser262, Arg264, Ser265, Lys276, Arg288, Arg347, and His425. His425 was observed to adopt multiple conformations among the eight IucA copies in the asymmetric unit. This may suggest that this residue plays a more dynamic role in the active site, potentially also interacting with the two other substrates citrate and ahLys. The Mg^{2+} ion is coordinated with apparent hexadentate geometry by three oxygen atoms in ATP's phosphate chain on one side, and on the opposing side

DOI: 10.1021/acs.biochem.6b00409
Biochemistry 2016, 55, 3559−3570

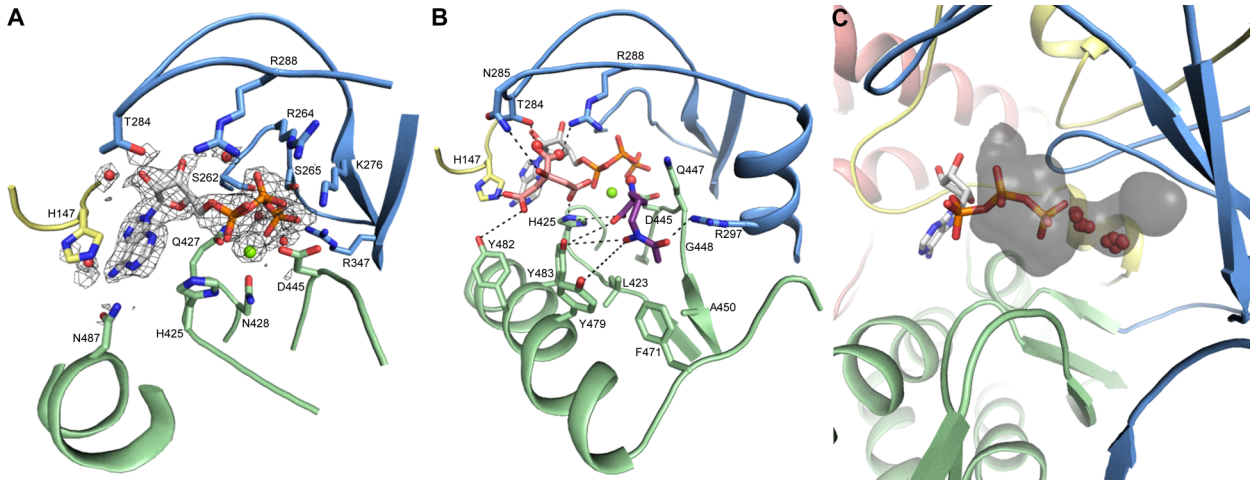

Figure 2. (A) A close-up representation of ATP (sticks, gray carbons) and Mg^{2+} (green sphere) in the active site of IucA. The unbiased $F_O - F_C$ electron density found in the active site calculated prior to inclusion of ATP contoured at 2.5σ is included (gray mesh). The enzyme side chains (sticks, colored by heteroatom) proposed to be important for coordinating ATP and Mg^{2+} are labeled. Water molecules are shown as red spheres. (B) A proposed quaternary model of the active site of IucA populated by its three native substrates ATP (gray), citrate (salmon), and ahLys (purple). Citrate was manually placed using the conformation from AcsD (2W03) to coincide with two ordered water molecules. The nucleophile ahLys was modeled by *in silico* docking into the ternary model. Residues thought to be important for binding citrate and ahLys are labeled. Postulated hydrogen bonds between citrate and ahLys, and enzyme side chains are represented by dashed lines. (C) A depiction of the potential PP_i displacement cavity in IucA. A solvent accessible tunnel (semitransparent gray surface) encloses the β- and γ-phosphates of ATP and extends out from the phosphate chain. Two clusters of ordered water molecules from the eight protomers in the asymmetric unit are shown populating the cavity.

by the oxygens in the side chains of Gln427, Asn428, and Asp445.

Attempts to obtain a crystal structure of IucA coordinated with its other two substrates, citrate and ahLys, have been unsuccessful to date. However, we employed *in silico* docking and modeling to propose a model of how the substrates citrate and ahLys may bind in the active site of IucA (Figure 2B). In order to incorporate citrate in the active site, the identical binding pose of citrate in the active site of AcsD cocrystallized with adenosine, citrate, and sulfate (2W03) was borrowed and manually positioned so the oxygen atoms of the tertiary carboxyl group overlapped with two ordered water molecules found in the crystal structure. As in AcsD, this arrangement placed the reactive pro-*R* primary carboxyl in a satisfactory position to attack the α-phosphate of ATP to form the citryl adenylate intermediate.[28] In this binding pose, the carboxyl groups are positioned to hydrogen bond with T284, R288, H425, and Y482, all of which are conserved in AcsD. The hydroxyl group is positioned to potentially interact with N285, also present in AcsD, despite the side chain being unresolved in four of the eight protomers in the asymmetric unit. The actual binding of citrate in the active site would likely reduce side chain mobility and promote optimal side chain geometry around the substrate.

Next, we employed *in silico* docking[39] to investigate the binding pose of the nucleophile ahLys. While it is currently unclear whether ahLys binds to the IucA·ATP·citrate or IucA·citryl-adenylate·PP_i complex (or both), we employed the IucA:ATP:citrate model described above as the receptor for the docking of ahLys. Of all the possible binding modes predicted, a large proportion placed the reactive primary amino group of ahLys in a position that overlapped with an ordered water molecule in the active site. A plausible binding conformation for ahLys identified in our docking studies is presented in Figure 2B. In this pose, the reactive primary amino group overlaps with the ordered water and is in a feasible position to attack the reactive carbonyl of the citryl-adenylate intermediate. The carboxyl group is pointed downward to hydrogen bond with His425 and Tyr483. The hydroxamate is positioned to hydrogen bond with Tyr483 and Tyr479, while the carbonyl is directed toward Arg297. The aliphatic backbone and methyl group of ahLys can favorably interact with a shallow hydrophobic groove outlined by Leu423, Gln447, Gly448, Ala450, and Phe471. Again, the "induced fit" of actual substrate binding is likely to alter local active site geometry in order to optimize binding and catalysis. While the proposed binding modes for citrate and ahLys from our docking studies are credible from a structural point of view and provide an initial working model, the actual conformations of these ligands in IucA's active site need to be evaluated further with both structural and functional studies.

Previous work has guided the theory that NIS synthetases do not immediately release PP_i following the first partial reaction that forms the adenylate intermediate (Scheme 1B). Kadi and Challis demonstrated that the PP_i exchange assay is not suitable for measuring the adenylate forming partial reaction in NIS synthetases.[45] This lack of PP_i exchange assay activity was also observed with IucA (data not shown). Corroborating this functional observation, a "PP_i displacement cavity" was identified in the crystal structure of AcsD that was proposed to accommodate the PP_i that is produced following the first partial reaction.[28] Consistent with this theory, our IucA with ATP crystal structure has a solvent-accessible tunnel encompassing and extending out from the β- and γ-phosphate of ATP that could potentially accept the PP_i displaced following adenylate-forming partial reaction (Figure 2C). The cavity contains two ordered waters molecules that could approximate the position of the γ-phosphate once it is displaced. The PP_i could be held here until the second partial reaction is completed and all of the final products vacate the active site.

Oligomeric State & Quaternary Structure. The published crystal structures of AcsD, AsbB, and AlcC suggest

DOI: 10.1021/acs.biochem.6b00409
Biochemistry 2016, 55, 3559−3570

that these homologous NIS synthetases are biological dimers (Figure 3A).[26,28] However, despite all being dimers, the Type A and Type C NIS synthetases display significantly different quaternary structures and dimer interfaces. Computational analysis (PISA[47]) of our IucA crystal structures failed to identify any biologically significant interfaces, and consequently predicted that IucA exists as a biological monomer. The SDS-PAGE image of purified IucA displayed in Figure 4A shows that IucA runs marginally below its predicted monomeric molecular mass of 64.9 kDa. However, native gel electrophoresis showed that IucA migrated close to the 242 kDa molecular weight marker (Figure 4B). Furthermore, size exclusion chromatography of purified IucA predicted that it had a molecular mass of 240 kDa (Figure 4C). With computational analysis of our crystal structures predicting a monomer, biochemical data most consistent with a tetramer, and three NIS synthetase homologues all reported to be biological dimers, we employed SAXS analysis to better characterize the oligomeric state and quaternary structure of IucA.

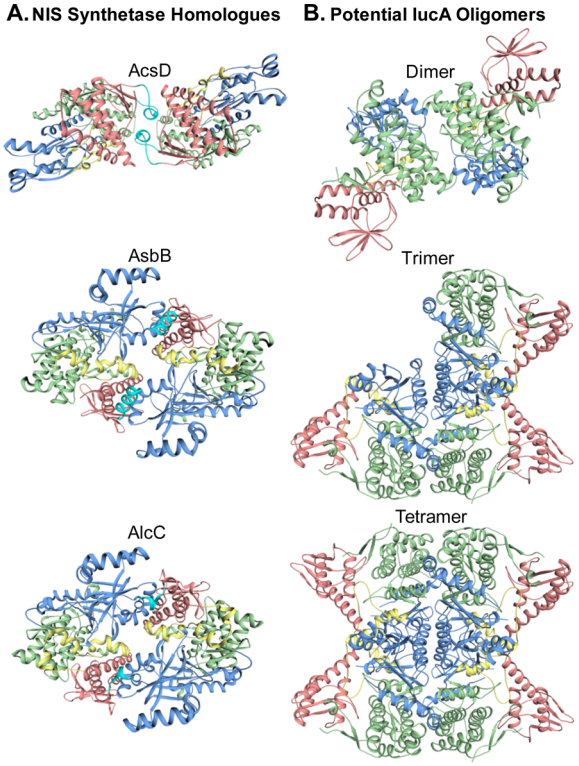

Figure 3. (A) The dimeric biological assemblies of three structurally characterized NIS synthetases: AcsD (2W02), AsbB (3TO3), and AlcC (2X0Q). Proposed "dimer defining" regions are highlighted in cyan. (B) Three potential oligomeric assemblies of IucA extracted from the IucA crystal structure. The tetramer is composed of two dimers.

The molecular weight and size values calculated from the SAXS analysis of IucA are presented in Table 2. The molecular weights predicted from the SAXS curves using three distinct methods are decidedly consistent with the molecular weight estimates from SEC and native gel electrophoresis, all centered around ~240 kDa. Despite marginally underestimating the theoretical tetrameric molecular mass of 259.6 kDa, these molecular mass estimates are all most consistent with that of a tetramer. With only eight residues unresolved on the N-terminus, and two amino acids unresolved on the C-terminus in the IucA crystal structures, it is unlikely that the slightly underestimated molecular weight of IucA is the result of protein truncation, but more likely a consequence of how unique protein properties such as particle size and shape can influence these mass determination techniques.

In order to better characterize the quaternary structure of this proposed tetramer, we examined the crystal packing in the IucA crystal and extracted the potential dimeric and tetrameric arrangements shown in Figure 3B. Because the molecular weight estimates tended to underestimate the predicted tetrameric weight, an asymmetric trimeric model was also included for completeness. Using CRYSOL software, we calculated the scattering curves of these potential oligomers and compared them to the experimental scattering curve of IucA (Figure 5A). The superb agreement between the curve predicted from the tetramer and the experiment curve suggests that IucA exists nearly exclusively as this tetrameric assembly in solution. To further support this conclusion, a representative *ab initio* molecular envelope was calculated from the SAXS data (Figure 6). Features in the molecular envelope, such as its

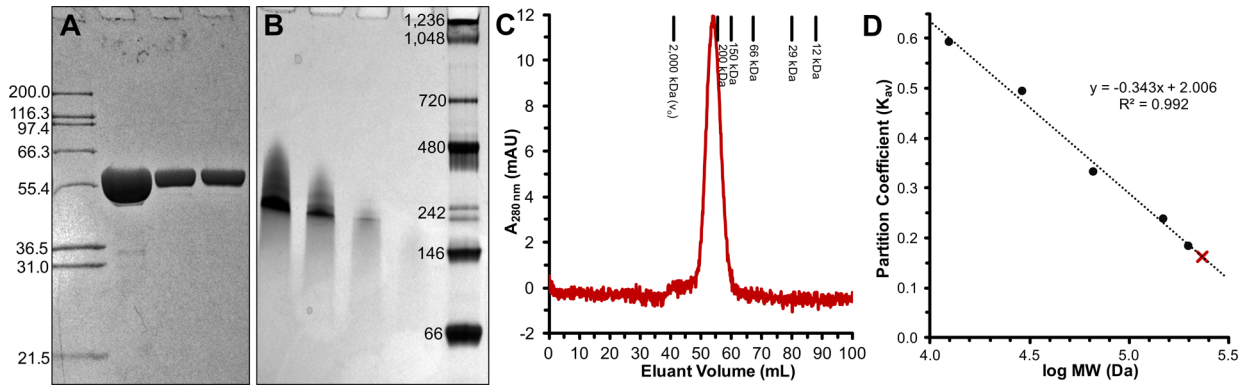

Figure 4. (A) A 12% SDS-PAGE gel of three IucA fractions of unknown concentration following IMAC purification and N-terminal His-tag cleavage. IucA has a theoretical molecular mass of 64.9 kDa. (B) Native gel (4–20%) electrophoresis of three concentrations (1.5, 0.75, and 0.375 mg/mL) of purified IucA. IucA migrated near the 242 kDa marker. (C) Size exclusion chromatogram of purified IucA. The tick marks at the top of the chromatogram correspond to the elution volume of protein standards. (D) The molecular weight standard curve generated from the protein standards in the previous panel. The 53.8 mL elution volume of IucA corresponds to a predicted molecular mass of 240 kDa, which is depicted by a red "X" on the standard curve.

DOI: 10.1021/acs.biochem.6b00409
Biochemistry 2016, 55, 3559–3570

Table 2. IucA Particle Size and Mass by SAXS[a]

	R_G by $P(r)$ (Å)	D_{MAX} by $P(r)$ (Å)	M.W. by I_0 (kDa)	M.W. by PV (kDa)	M.W. by V_C (kDa)
[IucA] (mg/mL)					
5.30	41.0	128	235	236	238
3.98	41.4	131	231	239	240
2.65	41.7	131	240	243	241
1.33	41.7	131	256	248	241
mean ± SD	41.5 ± 0.4	130 ± 2	240 ± 11	241 ± 5	240 ± 1
0[b]	41.9	134	240	244	242
[IucA] w/ATP (mg/mL)					
5.05	40.8	130	235	220	233
3.79	41.0	129	234	223	234
2.53	41.3	132	241	228	235
1.26	41.5	130	231	232	235
mean ± SD	41.2 ± 0.3	130 ± 1	235 ± 4	226 ± 5	234 ± 1
0[b]	41.6	133	242	232	238

[a] R_G = radius of gyration, D_{MAX} = maximum particle dimension, $P(r)$ = pair distance distribution, I_0 = zero-angle scattering intensity, PV = Porod volume, and V_C = volume of correlation. [b] To correct for any minor concentration dependence, particle size and mass values were also calculated for scattering data extrapolated to infinite dilution.

overall "X" shape and its central cavity, convincingly correlate with the tetrameric crystal structure.

To investigate if the binding of ATP to IucA induces a conformational or oligomeric change in solution, SAXS data were also collected in the presence of 1 mM ATP and $MgCl_2$. As can be seen in the particle size data in Table 2, interaction with ATP does not cause a significant change in particle dimensions or predicted molecular weight. However, a small, but clearly detectable conformational change is evidenced by differences in the experimental scattering curves presented in Figure 5B. The differences in the experimental SAXS curves are also mirrored by the scattering curves calculated from the two tetrameric crystal structures, suggesting that the small conformation change detected in solution was also captured *in crystallo*. Superposition of the two tetrameric crystal structures does not reveal any extensive structural differences (0.53 Å RMSD over 1830 α-carbons). However, the conformation change detected in the SAXS curves could correspond to more subtle structural differences, such as the changes in the "lid" loop discussed above.

IucA Activity. The specificity of IucA with respect to carboxylic acid and nucleophile substrate was probed using two activity assays. A ferric hydroxamate assay[45,46] was used to show that IucA has a clear preference for citrate as its carboxylic acid substrate (Figure 7A). This result is consistent with the stereospecific citrate binding mode originally described by Schmelz et al. (and illustrated in Figure 2B), where all three of the nonreactive polar functional groups of citrate hydrogen bond with conserved residues.[28] Because the native nucleophile substrate ahLys is not commercially available, we investigated the activity of IucA with other analogues and the simple nucleophile hydroxylamine using a coupled NADH consumption assay (Figure 7B). Of the substrates tested, hydroxylamine yielded the greatest activity. Surprisingly, L-lysine showed no detectable activity. However, addition of an acetyl group to the N^6 position of lysine restored about half the activity of hydroxylamine. It seems logical that also adding the hydroxyl group to the N^6 position, as in the native nucleophile ahLys, would further restore activity. Because ahLys and L-lysine share the same reactive primary amino group, the ability of IucA to discriminate between the two must lie in its ability to form specific binding interactions with the N^6 acetyl and hydroxyl groups, which are remote from the reactive end of the molecule. While the binding mode that we propose in Figure 2B includes specific interactions with the N^6 acetyl and hydroxyl groups, additional experiments are required to probe how this striking discrimination is truly achieved.

Apparent kinetic parameters were determined for IucA with multiple substrates using the NADH consumption assay. The enzyme saturation curves used to derive the kinetic parameters are displayed in Figure 8. The Michaelis constant, turnover number, and catalytic efficiency for IucA with ATP, citrate, and the surrogate nucleophiles hydroxylamine and N^6-acetyllysine are tabulated in Table 3. As expected, IucA has a relatively strong affinity for its native substrates ATP and citrate, exhibiting K_M values of 130 ± 30 and 180 ± 30 μM, respectively. Consistent with being auxiliary nucleophiles, the affinity of IucA for hydroxylamine and N^6-acetyllysine was dramatically lower, having K_M values of 15 ± 6 and 25 ± 6 mM, respectively. For each substrate, IucA had a similar turnover number centered around 20 per minute.

DISCUSSION

In the present study, we report the X-ray crystal structure of the prototypical Type A NIS synthetase IucA, from a strain of hvKP. Despite only sharing ~20% sequence identity with its structurally characterized NIS synthetase homologues AcsD, AsbB, and AlcC, the four enzymes share remarkably similar monomeric tertiary structure. In addition, they appear to share very similar approaches for binding their common substrate ATP. In this binding pose, ATP sits in a pocket deep within the active site, making specific interactions with the adenine, ribose, and phosphate components of the molecule (Figure 2A). Because we have yet to obtain a crystal structure of IucA complexed with citrate or its nucleophile ahLys, manual modeling and *in silico* docking allowed us to propose what IucA's quaternary active site may look like (Figure 2B). From a structural perspective, our model supports the hypothesis that ATP must bind to the active site first, followed by citrate. After the pro-*R* primary carboxyl of citrate attacks the α-phosphate of ATP to form the citryl-adenylate intermediate, our model also supports the theory that PP_i is displaced into a cavity containing ordered water molecules (Figure 2C), rather than being immediately released. However, the timing of nucleophile

DOI: 10.1021/acs.biochem.6b00409
Biochemistry 2016, 55, 3559−3570

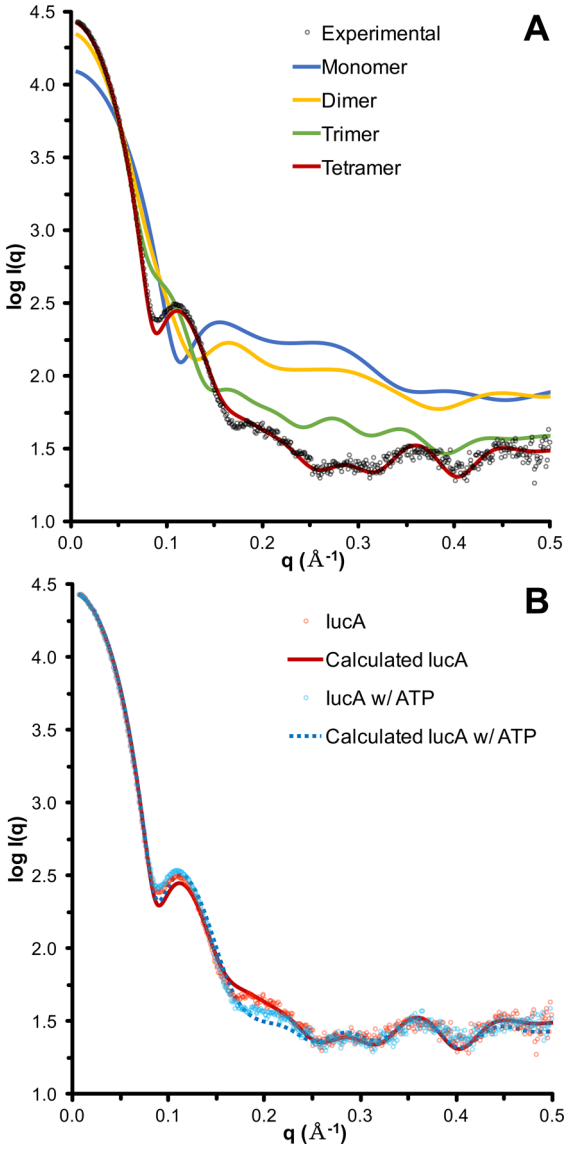

Figure 5. (A) The SAXS curves calculated from an IucA monomer, dimer, and trimer, and tetramer (shown in Figures 1 and 3B) found in the IucA crystal structure fitted to the experimental IucA scattering curve extrapolated to infinite dilution. (B) The experimental (extrapolated to infinite dilution) and calculated SAXS curves of tetrameric unliganded IucA, and tetrameric IucA with 1 mM ATP and $MgCl_2$.

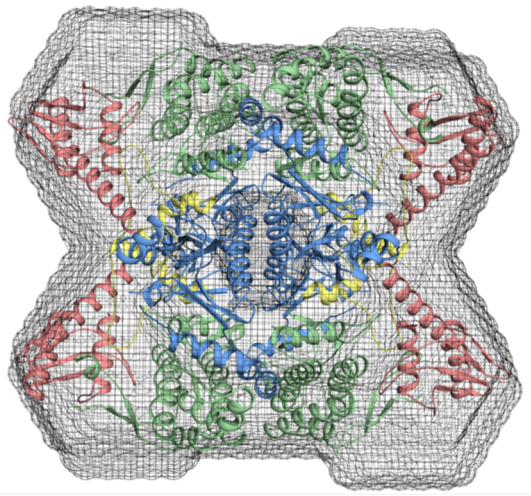

Figure 6. IucA crystal structure tetrameric assembly fitted inside a representative SAXS *ab initio* molecular envelope (gray mesh).

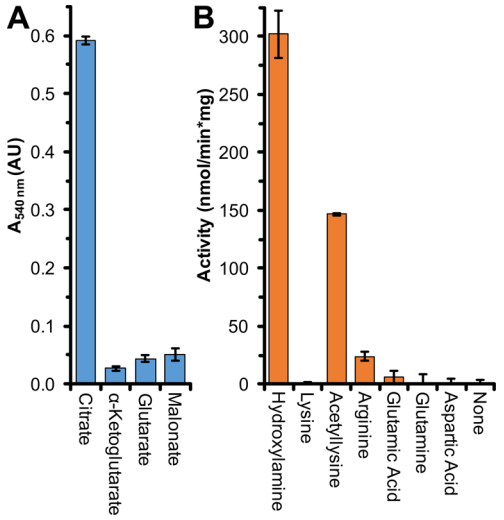

Figure 7. (A) The activity of IucA assayed with four possible carboxylic acid substrates using a ferric hydroxamate detection assay. Each bar represents the mean of seven reactions and error bars are ±1 SD. (B) The activity of IucA measured with a variety of possible nucleophile substrates using a NADH consumption assay. Each bar represents the mean of triplicate reactions and the error bars represent ±1 SD.

binding remains unresolved with regard to whether ahLys binds to the citryl-adenylate complex, or the ATP-citrate complex, or both. In any case, attack of the citryl-adenylate carbonyl by the primary amino group of ahLys yields the amide product citryl-ahLys and all products can be released from the enzyme.

IucA was shown to be very specific for its carboxylic acid substrate citrate, showing very limited activity with other similar acids (Figure 7A). In contrast, IucA was somewhat more promiscuous in its nucleophile preference, showing substantial activity with the non-native substrates hydroxylamine and N^6-acetyllysine (Figure 7B). Quite surprisingly, IucA showed no detectable activity with L-lysine, suggesting that the enzyme possesses a robust mechanism for discriminating between the proteinogenic amino acid and its native substrate, lysine derivative ahLys. While our proposed quaternary active site model may provide some insight into how this discrimination is achieved, additional studies will be required to fully confirm it. IucA displayed substantial activity with the surrogate nucleophiles hydroxylamine and N^6-acetyllysine, but had relatively poor affinity for these substrates with K_M values in the 10−30 mM range. IucA's apparent affinity for citrate (K_M = 180 ± 30 μM) was substantially greater than its homologues AcsD and AsbB, which were reported to have K_M's of approximately 5 mM.[26,28] The substrate inhibition discussed by the authors may be partly responsible for the differences.

Computational analysis of our IucA crystal structures using PISA[47] predicted that IucA was a biological monomer. However, biochemical data suggested that IucA had a molecular weight close to that of a tetramer (Figure 4B,C). Furthermore, the homologous NIS synthetases AcsD, AsbB, and AlcC were all reported to be biological dimers (Figure 3A).[26,28] We used SAXS analysis of IucA to conclusively determine that IucA exists as a tetramer in solution. The tetrameric assembly found

DOI: 10.1021/acs.biochem.6b00409
Biochemistry 2016, 55, 3559−3570

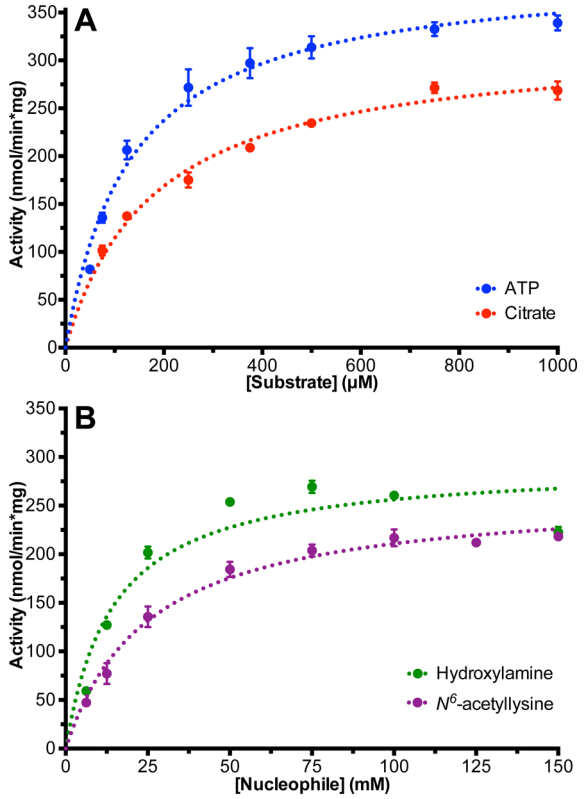

Figure 8. (A) A plot of IucA activity versus the concentration of native substrates ATP and citrate. Each data point represents the mean of triplicate reactions and the error bars represent ±1 SEM. The data points were fit with best-fit nonlinear regression lines (dotted line) to approximate the apparent kinetic parameters K_M and V_{MAX}. (B) A plot of IucA activity versus concentration of surrogate substrates hydroxylamine and N^6-acetyllysine.

Table 3. Apparent IucA Steady State Kinetic Parameters[a]

substrate	V_{MAX} (μM/min)	K_M (μM)	k_{cat} (min^{-1})	k_{cat}/K_M (M^{-1} s^{-1})
ATP	52 ± 2	130 ± 30	26 ± 1	3200
citrate	42 ± 1	180 ± 30	21 ± 1	1900
hydroxylamine	38 ± 2	15000 ± 6000	19 ± 1	22
N^6-acetyllysine	34 ± 1	25000 ± 6000	17 ± 1	11

[a] V_{MAX}, K_M, and k_{cat} are nonlinear regression best fit values ±1 SEM.

in solution corresponds closely with the crystal packing found in both IucA crystal structures (Figures 5A and 6).

The varied oligomeric state and quaternary structure of these four structurally characterized NIS synthetases is quite striking, raising several questions: What causes it, and what, if any, biological significance could it have? It appears that the sequence and structure of the thumb domains play a principle role in determining quaternary structure. The sequence of the thumb domains among these four homologues is less conserved than the other two domains and contains several insertions and deletions. Also, the fact that the thumb domains do not contribute any residues to the active site hints that the thumb domain plays more of a structural rather than catalytic role. Comparison of the dimer interfaces of the NIS synthetases in Figure 3A reveals a couple "dimer defining" features within the thumb domains. The dimer interface in AcsD is dominated by a loop (41−61) containing a turn of α-helix, which is not present in the other three synthetases. AsbB and AlcC share a nearly identical dimer interface, which includes a key N-terminal stretch of α-helix (1−13 and 8−18, respectively) not found in the crystal structures of either IucA or AcsD. IucA, which lacks both of these key "dimer defining" features in our crystal structures, adopts a tetrameric assembly instead of forming a dimer. In this tetrameric assembly, the interfaces appear to be dominated mainly by the fingers domain, thumb domain, and the EL region between the thumb and fingers domains. With this structural knowledge in hand, one can envision how specific insertions/deletions in the *N*-terminal thumb domain sequence could have led to the evolution of homologous enzymes that adopt such varied quaternary structure. It may also imply that it could be possible to alter the sequence of the thumb domain in order to engineer an NIS synthetase with a desired oligomeric state or quaternary structure.

At this time, it is not obvious what impact the NIS synthetase quaternary structure would have on their biological function. However, we will allude to a couple ideas where quaternary structure could play a role. First, in contrast to NRPS pathways, which shuttle intermediates from from active site to active site by covalent attachment to carrier domains,[48] NIS pathways lack a clear mechanism for efficiently transferring intermediates from one enzyme active site to the next. It is possible that the quaternary structure of the NIS enzymes is important for spatially organizing active sites in an arrangement that efficiently passes intermediates from active site to active site. Second, quaternary structure could potentially play a role in the cellular organization of NIS biosynthetic pathways. In a manner analogous to the multienzyme "siderosome" that has been proposed for the pyoverdine biosynthetic pathway,[49−51] it is possible that the aerobactin and other NIS pathways could also have a defined cellular organization where the quaternary structure of the component enzymes would certainly impact the assembly of multienzyme complexes.

A KP "superbug" with both hypervirulent and extreme drug resistant phenotypes poses a serious threat to the medical community that would likely require novel therapeutics to combat. With overproduction of the siderophore aerobactin being proposed as a principle mediator of the enhanced virulence of hvKP, the structural and functional characterization of IucA, a key biosynthetic enzyme required for aerobactin production, provides insight into a potential antivirulence therapeutic target that could disarm this dangerous pathogen. Furthermore, because aerobactin biosynthetic clusters are found in a number of pathogenic enteric Gram-negative bacteria, including *Escherichia*, *Salmonella*, *Shigella*, *Yersinia*, and *Citrobacter*, establishing a therapeutic target against aerobactin is potentially that much more valuable. Beyond the potential therapeutic application, the structural and functional characterization of IucA further augments our knowledge of the relatively understudied family of NIS synthetases.

AUTHOR INFORMATION

Corresponding Author

*Address: The Hauptman-Woodward Medical Research Institute, 700 Ellicott Street, Buffalo, NY, 14203-1102. E-mail: gulick@hwi.buffalo.edu. Phone: (716) 898-8619.

Funding

This research was supported by the National Institutes of Health (AI116998 to A.M.G.) and pilot studies support from the Buffalo Clinical and Translational Research Center (NIH Grant UL1TR001412 (PI, Dr. Timothy F. Murphy)). D.C.B.

DOI: 10.1021/acs.biochem.6b00409
Biochemistry 2016, 55, 3559−3570

was supported by NIH Training Grant T32-AI007614 (PI, Dr. Laurie K. Read). Diffraction data were collected at the GM/CA beamline of the Advanced Photon Source, which is funded by the National Cancer Institute (ACB-12002) and the National Institute of General Medical Sciences (AGM-12006) under Department of Energy Contract Number DE-AC02-06CH11357 to APS, and the Stanford Synchrotron Radiation Lightsource, a national user facility operated by Stanford University on behalf of the U.S. Department of Energy, Office of Basic Energy Sciences. The SSRL Structural Molecular Biology Program is supported by the Department of Energy, Office of Biological and Environmental Research, and by the NIH, NCRR, Biomedical Technology Program, and the National Institute of General Medical Sciences.

Notes

The authors declare no competing financial interest.

■ ACKNOWLEDGMENTS

We would like to thank Dr. Edward H. Snell for collecting the SAXS data on our IucA samples and Mathew R. Rice for helping grow and harvest IucA crystals.

■ REFERENCES

(1) Andrews, S. C., Robinson, A. K., and Rodríguez-Quiñones, F. (2003) Bacterial iron homeostasis. *FEMS Microbiology Reviews 27*, 215−237.

(2) Raymond, K. N., Dertz, E. A., and Kim, S. S. (2003) Enterobactin: an archetype for microbial iron transport. *Proc. Natl. Acad. Sci. U. S. A. 100*, 3584−3588.

(3) Parrow, N. L., Fleming, R. E., and Minnick, M. F. (2013) Sequestration and scavenging of iron in infection. *Infect. Immun. 81*, 3503−3514.

(4) Ong, S. T., Shan Ho, J. Z., Ho, B., and Ding, J. L. (2006) Iron-withholding strategy in innate immunity. *Immunobiology 211*, 295−314.

(5) Lamb, A. L. (2015) Breaking a pathogen's iron will: Inhibiting siderophore production as an antimicrobial strategy. *Biochim. Biophys. Acta, Proteins Proteomics 1854*, 1054−1070.

(6) Chu, B. C., Garcia-Herrero, A., Johanson, T. H., Krewulak, K. D., Lau, C. K., Peacock, R. S., Slavinskaya, Z., and Vogel, H. J. (2010) Siderophore uptake in bacteria and the battle for iron with the host; a bird's eye view. *BioMetals 23*, 601−611.

(7) Miethke, M., and Marahiel, M. A. (2007) Siderophore-based iron acquisition and pathogen control. *Microbiology and Molecular Biology Reviews 71*, 413−451.

(8) Warner, P. J., Williams, P. H., Bindereif, A., and Neilands, J. B. (1981) ColV plasmid-specific aerobactin synthesis by invasive strains of Escherichia coli. *Infect. Immun. 33*, 540−545.

(9) Takase, H., Nitanai, H., Hoshino, K., and Otani, T. (2000) Impact of siderophore production on Pseudomonas aeruginosa infections in immunosuppressed mice. *Infect. Immun. 68*, 1834−1839.

(10) Lee, J. Y., Passalacqua, K. D., Hanna, P. C., and Sherman, D. H. (2011) Regulation of petrobactin and bacillibactin biosynthesis in Bacillus anthracis under iron and oxygen variation. *PLoS One 6*, e20777.

(11) De Voss, J. J., Rutter, K., Schroeder, B. G., Su, H., Zhu, Y., and Barry, C. E., 3rd (2000) The salicylate-derived mycobactin siderophores of Mycobacterium tuberculosis are essential for growth in macrophages. *Proc. Natl. Acad. Sci. U. S. A. 97*, 1252−1257.

(12) Perry, R. D., and Fetherston, J. D. (2011) Yersiniabactin iron uptake: mechanisms and role in Yersinia pestis pathogenesis. *Microbes Infect. 13*, 808−817.

(13) Nassif, X., and Sansonetti, P. J. (1986) Correlation of the virulence of Klebsiella pneumoniae K1 and K2 with the presence of a plasmid encoding aerobactin. *Infection Immunity 54*, 603−608.

(14) Podschun, R., and Ullmann, U. (1998) Klebsiella spp. as nosocomial pathogens: epidemiology, taxonomy, typing methods, and pathogenicity factors. *Clin. Microbiol. Rev. 11*, 589−603.

(15) Kuehn, B. M. (2013) "Nightmare" bacteria on the rise in US hospitals, long-term care facilities. *JAMA 309*, 1573−1574.

(16) Patel, P. K., Russo, T. A., and Karchmer, A. W. (2014) Hypervirulent Klebsiella pneumoniae. *Open Forum Infectious Diseases 1*, ofu028.

(17) Shon, A. S., Bajwa, R. P., and Russo, T. A. (2013) Hypervirulent (hypermucoviscous) Klebsiella pneumoniae: a new and dangerous breed. *Virulence 4*, 107−118.

(18) Shon, A. S., and Russo, T. A. (2012) Hypervirulent Klebsiella pneumoniae: the next superbug? *Future Microbiol. 7*, 669−671.

(19) Russo, T. A., Olson, R., Macdonald, U., Metzger, D., Maltese, L. M., Drake, E. J., and Gulick, A. M. (2014) Aerobactin mediates virulence and accounts for increased siderophore production under iron-limiting conditions by hypervirulent (hypermucoviscous) Klebsiella pneumoniae. *Infect. Immun. 82*, 2356−2367.

(20) Russo, T. A., Shon, A. S., Beanan, J. M., Olson, R., MacDonald, U., Pomakov, A. O., and Visitacion, M. P. (2011) Hypervirulent K. pneumoniae secretes more and more active iron-acquisition molecules than "classical" K. pneumoniae thereby enhancing its virulence. *PLoS One 6*, e26734.

(21) Russo, T. A., Olson, R., MacDonald, U., Beanan, J., and Davidson, B. A. (2015) Aerobactin, but not yersiniabactin, salmochelin and enterobactin, enables the growth/survival of hypervirulent (hypermucoviscous) Klebsiella pneumoniae ex vivo and in vivo. *Infect. Immun. 83*, 3325−3333.

(22) Gibson, F., and Magrath, D. I. (1969) The isolation and characterization of a hydroxamic acid (aerobactin) formed by Aerobacter aerogenes 62-I. *Biochim. Biophys. Acta, Gen. Subj. 192*, 175−184.

(23) Oves-Costales, D., Kadi, N., and Challis, G. L. (2009) The long-overlooked enzymology of a nonribosomal peptide synthetase-independent pathway for virulence-conferring siderophore biosynthesis. *Chem. Commun. (Cambridge, U. K.)*, 6530−6541.

(24) Challis, G. L. (2005) A widely distributed bacterial pathway for siderophore biosynthesis independent of nonribosomal peptide synthetases. *ChemBioChem 6*, 601−611.

(25) de Lorenzo, V., and Neilands, J. B. (1986) Characterization of iucA and iucC genes of the aerobactin system of plasmid ColV-K30 in *Escherichia coli*. *J. Bacteriol. 167*, 350−355.

(26) Nusca, T. D., Kim, Y., Maltseva, N., Lee, J. Y., Eschenfeldt, W., Stols, L., Schofield, M. M., Scaglione, J. B., Dixon, S. D., Oves-Costales, D., Challis, G. L., Hanna, P. C., Pfleger, B. F., Joachimiak, A., and Sherman, D. H. (2012) Functional and structural analysis of the siderophore synthetase AsbB through reconstitution of the petrobactin biosynthetic pathway from Bacillus anthracis. *J. Biol. Chem. 287*, 16058−16072.

(27) Schmelz, S., Botting, C. H., Song, L., Kadi, N. F., Challis, G. L., and Naismith, J. H. (2011) Structural basis for acyl acceptor specificity in the achromobactin biosynthetic enzyme AcsD. *J. Mol. Biol. 412*, 495−504.

(28) Schmelz, S., Kadi, N., McMahon, S. A., Song, L., Oves-Costales, D., Oke, M., Liu, H., Johnson, K. A., Carter, L. G., Botting, C. H., White, M. F., Challis, G. L., and Naismith, J. H. (2009) AcsD catalyzes enantioselective citrate desymmetrization in siderophore biosynthesis. *Nat. Chem. Biol. 5*, 174−182.

(29) Oves-Costales, D., Kadi, N., Fogg, M. J., Song, L., Wilson, K. S., and Challis, G. L. (2008) Petrobactin biosynthesis: AsbB catalyzes condensation of spermidine with N8-citryl-spermidine and its N1-(3,4-dihydroxybenzoyl) derivative. *Chem. Commun. (Cambridge, U. K.)*, 4034−4036.

(30) Russo, T. A., and Gill, S. R. (2013) Draft Genome Sequence of the Hypervirulent Klebsiella pneumoniae Strain hvKP1, Isolated in Buffalo, New York. *Genome Announcements 1*, e0006513.

(31) Clatworthy, A. E., Pierson, E., and Hung, D. T. (2007) Targeting virulence: a new paradigm for antimicrobial therapy. *Nat. Chem. Biol. 3*, 541−548.

DOI: 10.1021/acs.biochem.6b00409
Biochemistry 2016, 55, 3559−3570

(32) Doublie, S. (1997) Preparation of selenomethionyl proteins for phase determination. *Methods Enzymol. 276*, 523−530.
(33) Luft, J. R., Collins, R. J., Fehrman, N. A., Lauricella, A. M., Veatch, C. K., and DeTitta, G. T. (2003) A deliberate approach to screening for initial crystallization conditions of biological macromolecules. *J. Struct. Biol. 142*, 170−179.
(34) McCoy, A. J., Grosse-Kunstleve, R. W., Adams, P. D., Winn, M. D., Storoni, L. C., and Read, R. J. (2007) Phaser crystallographic software. *J. Appl. Crystallogr. 40*, 658−674.
(35) Leslie, A. G. W., and Powell, H. R. (2007) Processing diffraction data with mosflm, in *Evolving Methods for Macromolecular Crystallography: The Structural Path to the Understanding of the Mechanismof Action of CBRN Agents* (Read, R. J., and Sussman, J. L., Eds.), pp 41−51, Springer: Netherlands, Dordrecht.
(36) Terwilliger, T. C., Grosse-Kunstleve, R. W., Afonine, P. V., Moriarty, N. W., Zwart, P. H., Hung, L.-W., Read, R. J., and Adams, P. D. (2008) Iterative model building, structure refinement and density modification with the PHENIX AutoBuild wizard. *Acta Crystallogr., Sect. D: Biol. Crystallogr. 64*, 61−69.
(37) Emsley, P., and Cowtan, K. (2004) Coot: model-building tools for molecular graphics. *Acta Crystallogr., Sect. D: Biol. Crystallogr. 60*, 2126−2132.
(38) Afonine, P. V., Grosse-Kunstleve, R. W., Echols, N., Headd, J. J., Moriarty, N. W., Mustyakimov, M., Terwilliger, T. C., Urzhumtsev, A., Zwart, P. H., and Adams, P. D. (2012) Towards automated crystallographic structure refinement with phenix.refine. *Acta Crystallogr., Sect. D: Biol. Crystallogr. 68*, 352−367.
(39) Trott, O., and Olson, A. J. (2010) AutoDock Vina: improving the speed and accuracy of docking with a new scoring function, efficient optimization, and multithreading. *J. Comput. Chem. 31*, 455−461.
(40) Martel, A., Liu, P., Weiss, T. M., Niebuhr, M., and Tsuruta, H. (2012) An integrated high-throughput data acquisition system for biological solution X-ray scattering studies. *J. Synchrotron Radiat. 19*, 431−434.
(41) Smolsky, I. L., Liu, P., Niebuhr, M., Ito, K., Weiss, T. M., and Tsuruta, H. (2007) Biological small-angle X-ray scattering facility at the Stanford Synchrotron Radiation Laboratory. *J. Appl. Crystallogr. 40*, s453−s458.
(42) Petoukhov, M. V., Franke, D., Shkumatov, A. V., Tria, G., Kikhney, A. G., Gajda, M., Gorba, C., Mertens, H. D. T., Konarev, P. V., and Svergun, D. I. (2012) New developments in the ATSAS program package for small-angle scattering data analysis. *J. Appl. Crystallogr. 45*, 342−350.
(43) Grant, T. D., Luft, J. R., Carter, L. G., Matsui, T., Weiss, T. M., Martel, A., and Snell, E. H. (2015) The accurate assessment of small-angle X-ray scattering data. *Acta Crystallogr., Sect. D: Biol. Crystallogr. 71*, 45−56.
(44) Wu, M. X., and Hill, K. A. (1993) A continuous spectrophotometric assay for the aminoacylation of transfer RNA by alanyl-transfer RNA synthetase. *Anal. Biochem. 211*, 320−323.
(45) Kadi, N., and Challis, G. L. (2009) Siderophore biosynthesis a substrate specificity assay for nonribosomal peptide synthetase-independent siderophore synthetases involving trapping of acyl-adenylate intermediates with hydroxylamine. *Methods Enzymol. 458*, 431−457.
(46) Lipmann, F., and Tuttle, L. C. (1945) Specific micromethod for the determination of acyl phosphates. *J. Biol. Chem. 159*, 21−28.
(47) Krissinel, E., and Henrick, K. (2007) Inference of macromolecular assemblies from crystalline state. *J. Mol. Biol. 372*, 774−797.
(48) Drake, E. J., Miller, B. R., Shi, C., Tarrasch, J. T., Sundlov, J. A., Allen, C. L., Skiniotis, G., Aldrich, C. C., and Gulick, A. M. (2016) Structures of two distinct conformations of holo-non-ribosomal peptide synthetases. *Nature 529*, 235−238.
(49) Gasser, V., Guillon, L., Cunrath, O., and Schalk, I. J. (2015) Cellular organization of siderophore biosynthesis in Pseudomonas aeruginosa: Evidence for siderosomes. *J. Inorg. Biochem. 148*, 27−34.
(50) Imperi, F., and Visca, P. (2013) Subcellular localization of the pyoverdine biogenesis machinery of Pseudomonas aeruginosa: A membrane-associated "siderosome. *FEBS Lett. 587*, 3387−3391.
(51) Guillon, L., El Mecherki, M., Altenburger, S., Graumann, P. L., and Schalk, I. J. (2012) High cellular organization of pyoverdine biosynthesis in Pseudomonas aeruginosa: clustering of PvdA at the old cell pole. *Environ. Microbiol. 14*, 1982−1994.

DOI: 10.1021/acs.biochem.6b00409
Biochemistry 2016, 55, 3559−3570